Decoupled Dead-Time Compensation Method Using Revised-Resonant Control-Based Disturbance Observer in PMSM Drives

Jiewen Lang, Chengde Tong, *Member, IEEE*, Yuhong Zheng, Jingang Bai, *Member, IEEE*, and Ping Zheng, *Senior Member, IEEE*

***Abstract*—This article presents a decoupled dead-time compensation method for voltage source inverters in permanent magnet synchronous machine (PMSM) drives. In the proportional-integral-resonant (PIR) based compensation scheme, the performances of the current control loop and dead-time compensation are coupled. Hence, effective compensation of the dead-time effect is yield with the expense of distorted current step response, where significant overshoot and oscillation are introduced. Besides, the extended-state observer (ESO) based scheme suffers from poor compensation capability due to limited tracking bandwidth. To increase the tracking bandwidth, the quasi-resonant-controller (QRC) based disturbance observer was proposed. However, such observer suffers from the problem of system instability. To address above issues, a revised-resonant control-based disturbance observer is proposed in this article, which could fully decouple the performances of the current control loop and dead-time compensation. Compared with the PIR, the proposed scheme could donate superior compensation capability without introducing overshoot and oscillation in the current step response. Compared with the ESO, the proposed scheme could increase tracking bandwidth and thus donate superior compensation capability. Compared with the QRC-based observer, the proposed scheme could guarantee system stability. Detailed analysis of system stability and compensation capability is presented. Finally, the proposed scheme is experimentally validated on a 0.55 kW PMSM platform.**

***Index Terms*—Dead-time compensation, disturbance observer, permanent magnet synchronous machine (PMSM), resonant control.**

I. Introduction

THREE-PHASE pulsewidth modulation (PWM) voltage source inverters (VSIs) have been widely used in permanent magnet synchronous machine (PMSM) drives. To prevent short-through problem, a dead time interval is inserted into gate drive PWM signals. However, due to the dead-time effect, there exists inevitable error between the voltage reference and actual voltage output, leading to distortion in phase currents, and torque ripple. As a result, the dead-time effect would deteriorate the performance of the PMSM drive system. To address this issue, various dead-time compensation methods have been proposed, which can be mainly divided into three categories.

The first category is based on the average value theory [1], where the dead time induced voltage error is directly calculated and then compensated [2]. Such schemes virtually operate in an open-loop style, thus show excessive dependence on the model accuracy. Accurate models of the dead-time effect accounting for the parasitic capacitance were presented in [3], [4], and [5]. Besides, model-independent methods were proposed, which are based on the look up table [6], and terminal voltage measurement [7]. However, correspondingly, onerous experiments and additional hardware cost would be introduced. Despite the contributions, the average value theory based methods are still dependent on precise current polarity detection especially in the zero-crossing region. To address this issue, in [8], a high accuracy current polarity detection solution based on extra circuits was proposed. However, both hardware cost and complexity are increased.

The second category is based on suppression of the dead time induced specific current harmonics. In [9] and [10], the second-order generalized integrator and the adaptive linear neuron were utilized to extract the dead time induced sixth current harmonics, respectively. However, since extra controllers are needed to calculate the feedforward compensated voltage from the current harmonics, these methods are relatively complicated.

In addition, internal model controllers, including the resonant and repetitive controllers, were used to attenuate the dead time induced sixth current harmonics [11], [12], [13], [14], [15]. In [11], [12], [13], and [14], the proportional-integral (PI) current controller (i.e., the control law) was modified by embedding a quasi-resonant-controller (QRC) in parallel, i.e., the proportional-integral-resonant (PIR) controller. However, the current loop step response is distorted with significant overshoot and oscillation [12], [13]. Besides, since the performances of the current control loop and dead-time compensation are influenced and thus coupled by the QRC, a tradeoff between the dynamic- and steady-state performances is necessary when

Received 9 May 2024; revised 29 July 2024; accepted 7 September 2024. Date of publication 11 September 2024; date of current version 12 December 2024. This work was supported by the National Natural Science Foundation of China under Grant 52277044, Grant 51991385, Grant U2141225, and Grant 52437003. Recommended for publication by Associate Editor R. Kennel. *(Corresponding authors: Chengde Tong; Ping Zheng.)*

The authors are with the School of Electrical Engineering and Automation, Harbin Institute of Technology, Harbin 150001, China (e-mail: langjiewen@stu.hit.edu.cn; tongchengde@hit.edu.cn; 23b906036@stu.hit.edu.cn; baijingang@hit.edu.cn; zhengping@hit.edu.cn).

Color versions of one or more figures in this article are available at https://doi.org/10.1109/TPEL.2024.3458406.

Digital Object Identifier 10.1109/TPEL.2024.3458406

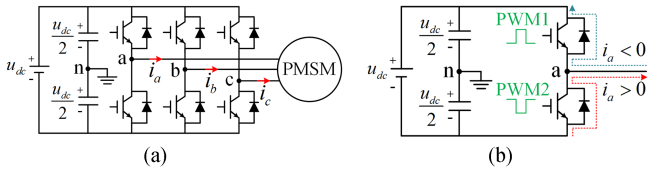

Fig. 1. PMSM drive system. (a) Three-phase PWM VSI with PMSM load. (b) Current flow direction during the dead time.

tuning control parameters. As a result, it is hard to improve the dynamic- and steady-state performances of the current response simultaneously. To address the issues, the partial prefilter-based and the dual-loop schemes were proposed in [16] and [17], respectively. However, despite contributions, the two schemes still suffer from the problems of coupled control parameters and system instability, respectively.

The third category is based on the concept of the disturbance observer, where the dead time induced voltage error is viewed as the system disturbance and thus estimated by the observer. In [18], [19], and [20], the extended-state observer (ESO) was employed for dead-time compensation. However, the ESO cannot track the dead time related high-frequency disturbance due to limited bandwidth [21], degrading the compensation performance. To increase the tracking bandwidth, the QRC was employed as the observer controller in [22]. However, it should be noted that the control law of [22] is the proportional controller. Hence, if the QRC-based observer presented in [22] is directly employed in the PI current controller-based scheme, undesired resonance phenomenon and consequent instability issue may arise, which is theoretically revealed in Section IV-C.

In this article, a decoupled dead-time compensation scheme is proposed. Instead of modifying the control law, a disturbance observer based on the revised-resonant control (RRC) is used to estimate and thus compensate the dead time induced voltage errors. The main contributions can be summarized as follows.

1) Compared with the PIR-based compensation scheme, the proposed scheme could fully decouple the performances of the current control loop and dead-time compensation. Hence, the dead-time compensation capability is enhanced significantly without distorting current step response. Specifically, undesired overshoot and oscillation in the PIR scheme are eliminated.
2) Compared with the ESO-based scheme, the proposed scheme could always donate superior tracking bandwidth and compensation capability in the entire speed range.
3) Compared with the QRC-based disturbance observer, the proposed RRC-based disturbance observer could eliminate the undesired resonance phenomenon completely. Thus, the system stability can be guaranteed in full frequency range.

The rest of this article is organized as follows. In Section II, the effect of dead time on VSI-based PMSM drives is analyzed. In Section III, the major drawbacks of the existing dead-time compensation methods are investigated. In Section IV, the proposed decoupled scheme is introduced, and the decoupling characteristic is verified in theory. In Section V, the stability and dead-time compensation capability are analyzed, based on which the parameter tuning method is discussed. In Section VI, experimental comparison results are presented to validate the proposed scheme. Finally, Section VII concludes this article.

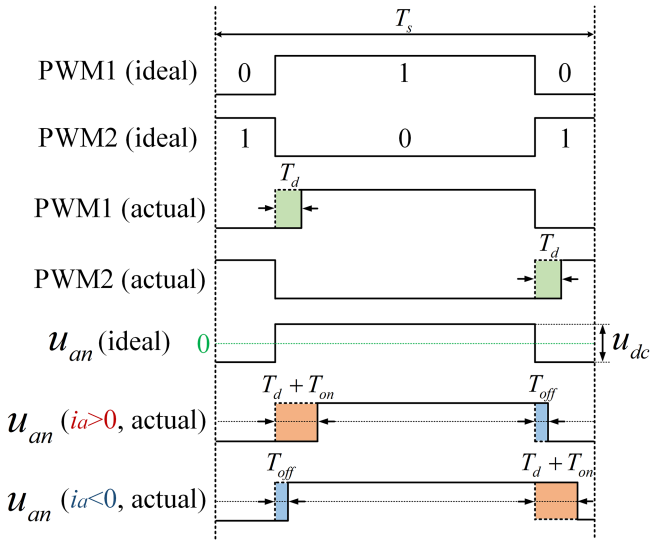

Fig. 2. Switching patterns and output voltage of one phase leg.

II. System Modeling

A. PMSM Model

In the d–q synchronous frame, the ideal mathematical model of the PMSM can be expressed as

$$\begin{cases} u_{ds} = R_s i_{ds} + L_d \frac{di_{ds}}{dt} - \omega_e L_q i_{qs} \\ u_{qs} = R_s i_{qs} + L_q \frac{di_{qs}}{dt} + \omega_e \left(L_d i_{ds} + \lambda_f \right) \end{cases} \tag{1}$$

where i_{ds} and i_{qs} are the d- and q-axis stator currents; u_{ds} and u_{qs} are the d- and q-axis stator voltages; L_d and L_q are the d- and q-axis inductances; R_s is the stator resistance; λ_f is the PM flux linkage; and ω_e is the electrical angular speed.

Assuming the machine is a surface-mounted PMSM, the dq-axes inductance is $L_{dq} = L_d = L_q$. For brevity, (1) can be rewritten in the form of d-q complex vector where $\boldsymbol{f}_{dqs} = f_{ds} + jf_{qs}$ as

$$\boldsymbol{u}_{dqs} = R_s \boldsymbol{i}_{dqs} + L_{dq} \frac{d\boldsymbol{i}_{dqs}}{dt} + \boldsymbol{u}_{cc} \tag{2}$$

where $\boldsymbol{u}_{cc}$ donates the cross-coupling term given by

$$\boldsymbol{u}_{cc} = -\omega_e L_q i_{qs} + j\omega_e \left(L_d i_{ds} + \lambda_f \right). \tag{3}$$

B. Dead-Time Effect Analysis

The typical three-phase PWM VSI with PMSM load is shown in Fig. 1(a), where insulated gate bipolar transistors (IGBTs) are adopted as the switching devices. The ideal switching patterns and corresponding output voltage are shown in Fig. 2.

However, due to inevitable turn-ON/OFF time delays (i.e., $T_{\rm on}$ and $T_{\rm off}$) of the IGBT, a dc-link short circuit would be caused. Therefore, to prevent short-through problem, the dead time T_d is

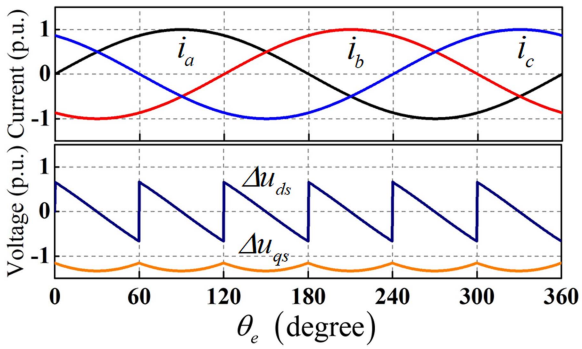

Fig. 3. Waveforms of the dead time induced voltage errors, where the base value of voltage is defined as: $(T_d+T_{\rm on}\text{-}T_{\rm off})u_{\rm dc}/T_s$.

inserted into gate drive PWM signals. As shown in Fig. 1(b), during the dead time, the phase current flows through the freewheeling diode, and the current path depends on the current direction. Thus, taking T_d, $T_{\rm on}$, and $T_{\rm off}$ into account, the actual gate drive PWM signals and corresponding output voltage are shown in Fig. 2. It is depicted that significant dead time induced voltage error is introduced in a-phase output voltage, which is given by

$$\Delta u_{an} = \frac{(T_d + T_{\rm on} - T_{\rm off})\, u_{\rm dc}}{T_s} \cdot \text{sign}(i_a) \tag{4}$$

where T_s and $u_{\rm dc}$ are the sampling (switching) period and the dc-link voltage, respectively; sign(i_a) can be expressed as

$$\text{sign}(i_a) = \begin{cases} 1, & i_a > 0 \\ -1, & i_a < 0 \end{cases}. \tag{5}$$

The voltage errors (Δu_{ds} and Δu_{qs}) in the d–q synchronous frame can be given by (6). Hence, according to (4), (5), and (6), the dead time induced voltage waveforms are shown in Fig. 3. Applying the Fourier series expansion, Δu_{ds} and Δu_{qs} can be expressed as (7). It is revealed that the dead-time effect mainly causes sixth voltage harmonic in the d–q synchronous frame. As a result, sixth current harmonic would be introduced, which can be mapped to fifth and seventh harmonics in the phase current [15]

$$\begin{bmatrix} \Delta u_{ds} \\ \Delta u_{qs} \end{bmatrix} = \frac{2}{3} \begin{bmatrix} \cos\theta_e & \cos(\theta_e - 2\pi/3) & \cos(\theta_e - 4\pi/3) \\ -\sin\theta_e & -\sin(\theta_e - 2\pi/3) & -\sin(\theta_e - 4\pi/3) \end{bmatrix} \times \begin{bmatrix} \Delta u_{an} \\ \Delta u_{bn} \\ \Delta u_{cn} \end{bmatrix} \tag{6}$$

where Δu_{bn} and Δu_{cn} are the voltage errors of b- and c-phases, respectively; θ_e is the electrical angle

$$\begin{cases} \Delta u_{ds} = \frac{4(T_d+T_{\rm on}-T_{\rm off})u_{\rm dc}}{\pi T_s} \sum_{n=1}^{\infty} \left[\frac{12n}{36n^2-1} \sin(6n\omega_e t)\right] \\ \Delta u_{qs} = \frac{4(T_d+T_{\rm on}-T_{\rm off})u_{\rm dc}}{\pi T_s} \left\{-1 + \sum_{n=1}^{\infty} \left[\frac{2}{36n^2-1} \cos(6n\omega_e t)\right]\right\} \end{cases}. \tag{7}$$

Considering the dead time induced voltage error $\Delta \boldsymbol{u}_{dqs}$, the PMSM model can be rewritten as

$$\boldsymbol{u}_{dqs} = R_s \boldsymbol{i}_{dqs} + L_{dq} \frac{d\boldsymbol{i}_{dqs}}{dt} + \boldsymbol{u}_{cc} - \Delta \boldsymbol{u}_{dqs}. \tag{8}$$

III. Existing Dead-Time Compensation Schemes and Its Drawbacks

The aforementioned analysis demonstrates that the dead-time effect would inevitably cause current harmonics, deteriorating the steady-state performance of the current loop. To address this issue, various dead-time compensation schemes are proposed. In this section, the performances of the conventional PI scheme, the PIR-based scheme, the ESO-based scheme, and the QRC-based disturbance observer are analyzed.

A. Conventional PI Scheme

In this article, as a widely used current control algorithm, the conventional PI scheme is chosen as the baseline, of which the block diagram is illustrated in Fig. 5 [the parallel QRC $G_{qrc}(s)$ is removed]. Then, the transfer functions of the current control loop and voltage disturbance rejection loop (from $\Delta \boldsymbol{u}_{dqs}$ to $\boldsymbol{i}_{dqs}$) can be deduced and given by (9) and (10), respectively. Corresponding Bode diagrams are shown in Fig. 7. It is shown by Fig. 7(b) that the gain of the voltage disturbance rejection loop is limited in high-frequency range. Hence, the PI controller cannot suppress the dead time induced high-frequency voltage harmonics effectively

$$G_{t1}(s) = \frac{\boldsymbol{i}_{dqs}(s)}{\boldsymbol{i}^*_{dqs}(s)} = \frac{K_p s + K_i}{L_{dq} s^2 + (K_p + R_s) s + K_i} \tag{9}$$

where K_p and K_i donate the proportional and integral coefficients of the PI current controller, respectively,

$$G_{d1}(s) = \frac{\boldsymbol{i}_{dqs}(s)}{\Delta \boldsymbol{u}_{dqs}(s)} = \frac{s}{L_{dq} s^2 + (K_p + R_s) s + K_i}. \tag{10}$$

B. PIR-Based Dead-Time Compensation Scheme

To solve the problem of dead-time effect, the conventional PI scheme is modified by embedding a parallel QRC current controller in the control law, as illustrated in Fig. 5 (the QRC is activated), i.e., the PIR-based dead-time compensation scheme.

The transfer function of the QRC can be expressed as

$$G_{qrc}(s) = \frac{2K_r \omega_c s}{s^2 + 2\omega_c s + \omega_0^2} \tag{11}$$

where K_r is the resonant coefficient; ω_0 and ω_c are the resonant and cutoff frequencies, respectively.

Based on the internal model theory, the resonant frequency of the QRC should be set to be the fundamental frequency of the voltage harmonics (i.e., $\omega_0 = 6\omega_e$). Fig. 4 presents the Bode diagram of the QRC with separate changes of K_r and ω_c. The QRC provides a peak gain at ω_0, which is proportional to K_r, as shown in Fig. 4(a). In addition, it is depicted by Fig. 4(b) that the bandwidth of the QRC increases with the raise of ω_c, while the peak gain is independent of ω_c. Hence, in the PIR scheme, to ensure sufficient compensation of the dead-time effect, the value of K_r is generally tuned to be relatively large.

From Fig. 5, the transfer functions of the current control and voltage disturbance rejection loops can be deduced and given by (12) and (13), respectively. According to (12) and (13), in the PIR scheme, the performances of both the current control

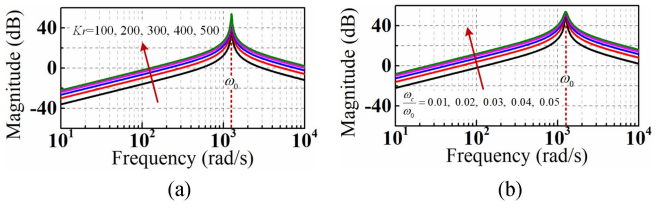

Fig. 4. Bode diagram of the QRC with separate changes of K_r and ω_c ($\omega_0 = 1257$ rad/s (200 Hz)). (a) $\omega_c = 0.01\omega_0$, K_r varies from 100 to 500. (b) $K_r = 500$, ω_c varies from 0.01 ω_0 to 0.05 ω_0.

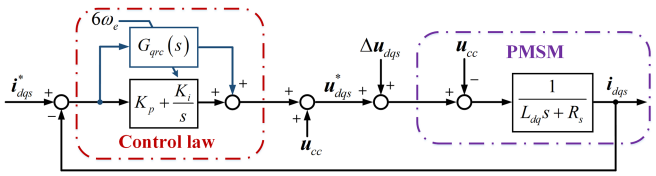

Fig. 5. Block diagram of the PIR-based compensation scheme.

and voltage disturbance rejection loops are directly influenced by the QRC parameters, i.e., the two loops are coupled. Hence, a compromise between the performances of the two loops is needed when tuning control parameters. As a result, it is hard to improve the dynamic- and steady-state performances of the current response simultaneously

$$G_{t2}(s) = \frac{\boldsymbol{i}_{dqs}(s)}{\boldsymbol{i}^*_{dqs}(s)} = \frac{(K_p + G_{qrc}(s))s + K_i}{L_{dq}s^2 + (K_p + R_s + G_{qrc}(s))s + K_i} \tag{12}$$

$$G_{d2}(s) = \frac{\boldsymbol{i}_{dqs}(s)}{\Delta\boldsymbol{u}_{dqs}(s)} = \frac{s}{L_{dq}s^2 + (K_p + R_s + G_{qrc}(s))s + K_i}. \tag{13}$$

The Bode diagrams of the PIR scheme are presented in Fig. 7. It is depicted by Fig. 7(b) that for the voltage disturbance rejection loop, the PIR controller donates a sharp drop in the magnitude at the resonant frequency, which can contribute to suppression of the dead time induced voltage error. However, compared with the PI scheme, the frequency characteristic of the current loop is significantly distorted due to the parallel QRC in the control law, as shown in Fig. 7(a). Specifically, a resonance phenomenon is introduced, leading to overshoot and oscillation in the current loop step response (see Fig. 11).

C. ESO-Based Dead-Time Compensation Scheme

In the ESO-based scheme, as illustrated in Fig. 6, the ESO is utilized to estimate and compensate the voltage disturbance. According to [18], the ESO gains h_1 and h_2 are designed as follows:

$$h_1 = 2\omega_{\text{eso}}, \quad h_2 = \omega^2_{\text{eso}} \tag{14}$$

where ω_{eso} donates the bandwidth of the ESO.

From Fig. 6, the transfer functions of the current control and voltage disturbance rejection loops can be given by (15) and (16),

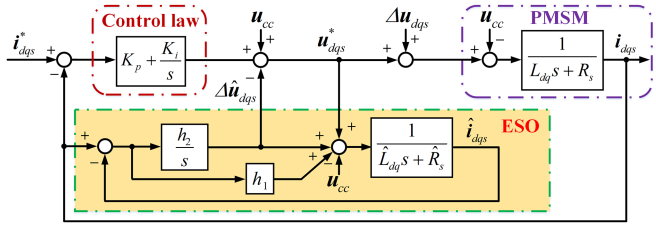

Fig. 6. Block diagram of the ESO-based compensation scheme.

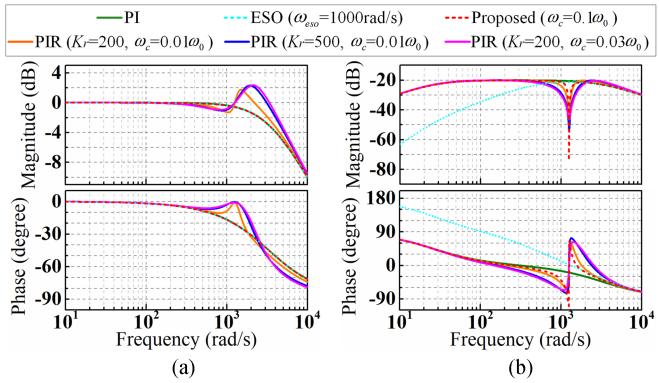

Fig. 7. Bode diagrams of the PI scheme, the PIR-based scheme, the ESO-based scheme, and the proposed scheme (L_{dq}= 3mH, $R_s = 0.08\Omega$, $K_p = 10$, $K_i = 267$, and $\omega_0 = 1257$ rad/s). (a) Current loop. (b) Disturbance loop.

respectively. It is revealed by (9) and (15) that the ESO-based scheme shares the same current loop transfer function as the PI scheme, which is independent of the ESO gains. Hence, the ESO could fully decouple the performances of the two loops

$$G_{t3}(s) = \frac{\boldsymbol{i}_{dqs}(s)}{\boldsymbol{i}^*_{dqs}(s)} = \frac{K_p s + K_i}{L_{dq}s^2 + (K_p + R_s)s + K_i} \tag{15}$$

$$G_{d3}(s) = \frac{\boldsymbol{i}_{dqs}(s)}{\Delta\boldsymbol{u}_{dqs}(s)} = \frac{s(L_{dq}s + R_s)}{L_{dq}s^2 + (h_1 + R_s)s + h_2} \cdot \frac{s}{L_{dq}s^2 + (K_p + R_s)s + K_i}. \tag{16}$$

In the ESO, since the raise of ω_{eso} would amplify the high-frequency noise and thus lead to system instability, ω_{eso} cannot be excessive high [21]. In this article, for a tradeoff between dynamics and stability margin, ω_{eso} is selected as 1000 rad/s. As shown by Fig. 7(b), the frequency response of the ESO scheme virtually coincides with that of the PI scheme at high frequency above ω_{eso}. Hence, due to limited bandwidth, the ESO-based scheme inevitably suffers from weak compensation capability.

D. QRC-Based Disturbance Observer

The block diagram of the QRC-based disturbance observer presented in [22] can be illustrated by Fig. 8, where the RRC should be replaced with the QRC. Hence, the transfer function of the current control loop can be given by (26). It is revealed that the QRC-based disturbance observer could fully decouple the current control and voltage disturbance rejection loops.

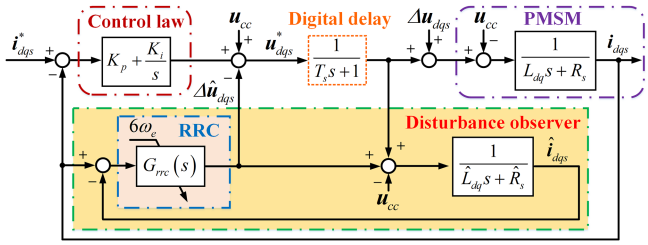

Fig. 8. Block diagram of the proposed scheme.

TABLE I
PERFORMANCE COMPARISON OF EXISTING DEAD-TIME COMPENSATION SCHEMES

Schemes	Coupling issue	Instability issue	Compensation performance
PI	No	No	Poor
PIR	Yes	No	Good
ESO	No	No	Poor
QRC-observer	No	Yes	Good

However, if the QRC-based disturbance observer is directly employed in the PI current controller-based scheme, undesired resonance phenomenon and consequent instability issue may arise, as shown in Fig. 12. Corresponding theoretical analysis is presented in Section IV-C.

In order to summarize and highlight the major drawbacks of the existing compensation schemes, a comparison is given in Table I. It is shown that the PI scheme suffers from the dead-time effect. Despite superior compensation capability, in the PIR scheme, due to the coupling issue, undesired overshoot and oscillation would be introduced in the current loop. While the ESO and the QRC-based disturbance observer enjoying the decoupling characteristic are subjected to weak compensation capability and system instability issue, respectively.

IV. DECOUPLED DEAD-TIME COMPENSATION SCHEME WITH RRC-BASED DISTURBANCE OBSERVER

To fully decouple the performances of the current control and voltage disturbance rejection loops, and address the problem of overshoot and oscillation in the current loop, in this article, a decoupled dead-time compensation scheme is proposed.

A. RRC-Based Disturbance Observer

The block diagram of the proposed dead-time compensation scheme is illustrated in Fig. 8. As shown, instead of modifying the control law, a disturbance observer is utilized for estimation and compensation of the dead time induced voltage disturbance. Hence, the basic control law of the PI scheme is retained. A Luenberger-style close-loop scheme is adopted in the observer, where an RRC is employed to track the ac voltage disturbance.

For simplicity, in following analysis, the digital delay that is simplified as a first-order filter in Fig. 8 is neglected. And the effect of the digital delay is discussed in Section IV-D.

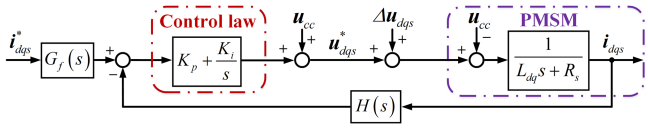

Fig. 9. Restructured block diagram of the proposed scheme.

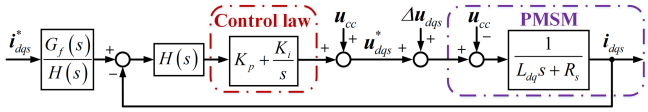

Fig. 10. Equivalent unit-feedback system.

The disturbance observer can be expressed as follows:

$$\Delta\hat{\boldsymbol{u}}_{dqs} = G_{oc}(s)\left(\boldsymbol{i}_{dqs} - \hat{\boldsymbol{i}}_{dqs}\right) \tag{17}$$

$$\hat{\boldsymbol{i}}_{dqs} = \left[\boldsymbol{u}^*_{dqs} - \boldsymbol{u}_{cc} + \Delta\hat{\boldsymbol{u}}_{dqs}\right]\frac{1}{\hat{L}_{dq}s + \hat{R}_s} \tag{18}$$

where $G_{oc}(s)$ is the transfer function of the observer controller;$\Delta\hat{\boldsymbol{u}}_{dqs}$ and $\hat{\boldsymbol{i}}_{dqs}$ represent the estimated voltage disturbance and estimated current, respectively; and $\hat{L}_{dq}$ and $\hat{R}_s$ donate the estimated dq-axes inductance and stator resistance, respectively.

B. Decoupling Characteristic

The transfer functions of the proposed scheme are derived to theoretically reveal the decoupling characteristic. According to Fig. 8, the voltage reference can be given by

$$\boldsymbol{u}^*_{dqs} = \left(K_p + \frac{K_i}{s}\right)\left(\boldsymbol{i}^*_{dqs} - \boldsymbol{i}_{dqs}\right) - \Delta\hat{\boldsymbol{u}}_{dqs} + \boldsymbol{u}_{cc}. \tag{19}$$

Substituting (17) and (18) into (19) yields

$$\boldsymbol{u}^*_{dqs} = \left[G_f(s)\,\boldsymbol{i}^*_{dqs} - H(s)\,\boldsymbol{i}_{dqs}\right]\left(K_p + \frac{K_i}{s}\right) + \boldsymbol{u}_{cc} \tag{20}$$

where $G_f(s)$ and $H(s)$ can be expressed as

$$G_f(s) = 1 + G_{oc}(s)\frac{1}{\hat{L}_{dq}s + \hat{R}_s} \tag{21}$$

$$H(s) = 1 + G_{oc}(s)\left(\frac{1}{K_p + K_i/s} + \frac{1}{\hat{L}_{dq}s + \hat{R}_s}\right). \tag{22}$$

According to (20), the block diagram of the proposed scheme can be reconstructed as Fig. 9. Then, the proposed scheme can be further simplified as an equivalent unit-feedback system, as shown in Fig. 10. From Fig. 10, the transfer functions of the current control and voltage disturbance rejection loops can be given as

$$G_{t4}(s) = \frac{\boldsymbol{i}_{dqs}(s)}{\boldsymbol{i}^*_{dqs}(s)} = \frac{G_f(s)}{H(s)} \cdot \frac{G_{\text{open}}(s)}{1 + G_{\text{open}}(s)} \tag{23}$$

$$G_{d4}(s) = \frac{\boldsymbol{i}_{dqs}(s)}{\Delta\boldsymbol{u}_{dqs}(s)} = \frac{1}{(L_{dq}s + R_s)\left[1 + G_{\text{open}}(s)\right]} \tag{24}$$

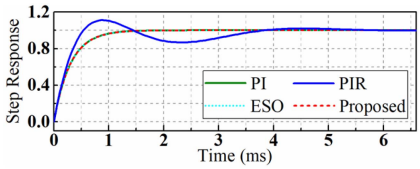

Fig. 11. Current loop step responses.

where

$$G_{\text{open}}(s) = H(s)\left(K_p + \frac{K_i}{s}\right)\frac{1}{L_{dq}s + R_s}. \tag{25}$$

Assuming all the estimated machine parameters are accurate (the effect of parameter mismatch is analyzed in Section IV-E), i.e., $\hat{L}_{dq} = L_{dq}$, $\hat{R}_s = R_s$, and substituting (21), (22), (25) into (23) and (24), then the transfer functions can be rewritten as

$$G_{t4}(s) = \frac{K_p s + K_i}{L_{dq}s^2 + (K_p + R_s)s + K_i} \tag{26}$$

$$G_{d4}(s) = \frac{L_{dq}s + R_s}{L_{dq}s + R_s + G_{oc}(s)} \cdot \frac{s}{L_{dq}s^2 + (K_p + R_s)s + K_i}. \tag{27}$$

From (9) and (26), it is demonstrated that the current loop transfer function of the proposed scheme is same as that of the PI scheme, which is independent of the observer parameters. Hence, based on such decoupling characteristic, the proposed scheme can fully decouple the performances of the current control and voltage disturbance rejection loops.

From (9), (12), (15), and (26), the current step responses of the four schemes can be obtained. As shown in Fig. 11, the step responses of the ESO-based and the proposed schemes coincide with that of the PI scheme showing the first-order characteristic. However, due to the aforementioned coupling issue, there exist significant overshoot and oscillation in the PIR scheme.

C. Revised-Resonant Controller

First, the shortcoming of the conventional QRC is analyzed. Enjoying the merit of superior performance in tracking AC signals, the QRC can be utilized as the observer controller [22], i.e., $G_{oc}(s) = G_{qrc}(s)$. In this condition, by (11) and (27), the Bode diagram of the disturbance loop $G_{d4}(s)$ is shown in Fig. 12. As expected, there exists sharp magnitude attenuation at the resonant frequency. However, above the resonant frequency, it is revealed that undesired resonant phenomenon is introduced, where the resonant peak even exceeds 0 dB. As a result, both unmodeled system disturbances and noise would be amplified, leading to system instability. As a result, the QRC-based disturbance observer that is presented in [22] cannot be directly employed in the PI current controller-based scheme.

To address this problem, a RRC is proposed as the observer controller. From (10) and (27), the disturbance loop transfer function of the proposed scheme can be rewritten as

$$G_{d4}(s) = G_{df}(s) \cdot G_{d1}(s) \tag{28}$$

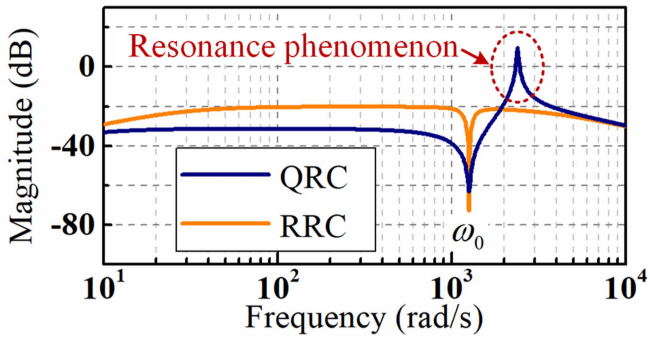

Fig. 12. Bode diagram of the disturbance loop in the proposed scheme with different observer controller.

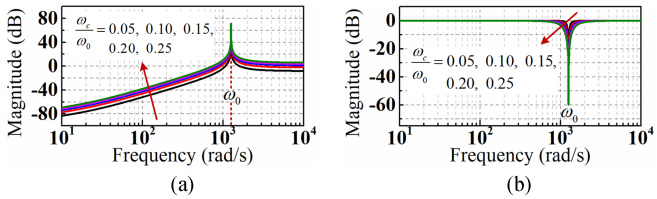

Fig. 13. Bode diagrams of the RRC $G_{rrc}(s)$ and the equivalent cascade filter $G_{df}(s)$ when ω_c varies from $0.05\omega_0$ to $0.25\omega_0$. (a) $G_{rrc}(s)$. (b) $G_{df}(s)$.

where $G_{df}(s)$ is given by

$$G_{df}(s) = \frac{L_{dq}s + R_s}{L_{dq}s + R_s + G_{oc}(s)}. \tag{29}$$

Hence, it is shown by (28) that compared with the PI scheme, the proposed disturbance observer functions as an equivalent cascade filter [i.e., $G_{df}(s)$] in the disturbance loop. In order to suppress the dead time induced voltage disturbances without deterioration in system stability, $G_{df}(s)$ is expected to exhibit a band-notch characteristic. Thus, in this paper, $G_{df}(s)$ is designed as a standard two-order notch filter, as show in

$$G_{df}(s) = \frac{s^2 + \omega_0^2}{s^2 + 2\omega_c s + \omega_0^2}. \tag{30}$$

From (29) and (30), the transfer function of the RRC can be deduced as

$$G_{rrc}(s) = G_{oc}(s) = \left(\hat{L}_{dq}s + \hat{R}_s\right)\frac{2\omega_c s}{s^2 + \omega_0^2}. \tag{31}$$

The Bode diagrams of the RRC $G_{rrc}(s)$ and the equivalent cascade filter $G_{df}(s)$ with the change of ω_c are shown in Fig. 13. The RRC donates a large gain at the resonant frequency, as shown in Fig. 13(a). At high-frequency range above ω_0, unlike the QRC where the gain descends with a slope of -20 dB/decade (see Fig. 4), the RRC converges to a constant gain near 0 dB.

From Fig. 13(b), as expected, the equivalent cascade filter $G_{df}(s)$ shows a band-notch characteristic. Substituting (31) into (27), the disturbance loop transfer function with the RRC can be given by (32), corresponding Bode diagram is shown in Fig. 12. It is demonstrated that undesired resonance phenomenon is eliminated completely by using the proposed RRC, thus the system stability can be guaranteed. Besides, at the resonant

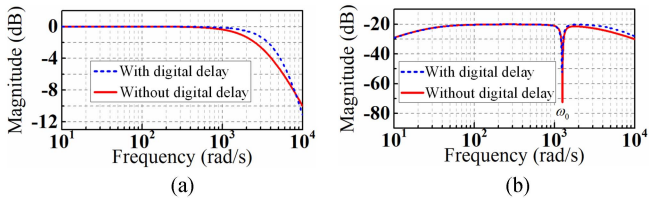

Fig. 14. Influence of the digital delay on the proposed scheme. (a) Current loop. (b) Disturbance loop.

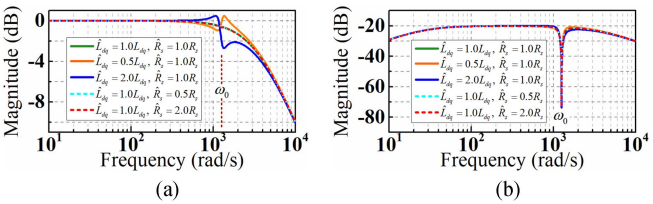

Fig. 15. Frequency responses of the proposed scheme under parameter mismatch. (a) Current loop. (b) Disturbance loop.

frequency, sharp magnitude attenuation is donated by the RRC, which can contribute to sufficient suppression of the dead time related voltage disturbances. Since the resonant frequency ω_0 is changed with speed adaptively, compared with the ESO-based scheme, the proposed scheme could always donate superior tracking bandwidth and compensation capability in the entire speed range, as shown by Fig. 7(b)

$$G_{d4}(s) = \frac{s^2+\omega_0^2}{s^2+2\omega_c s+\omega_0^2} \cdot \frac{s}{L_{dq}s^2+(K_p+R_s)s+K_i}. \tag{32}$$

D. Influence of Digital Delay

The influence of the digital delay on the proposed scheme is shown in Fig. 14. It is demonstrated that neglecting the digital delay would only introduce slight deviation at high frequency above 1000 rad/s. Besides, when taking the digital delay into account, the current loop still exhibits smooth response without resonance, while the disturbance loop could ensure sufficient suppression of the specific high-frequency harmonic. Hence, the digital delay is negligible within the rated speed range. It should be noticed that the stability margin would deteriorate slightly due to the digital delay.

E. Parameter Mismatch

As shown by Fig. 8 and (31), the proposed scheme relies on the estimated machine parameters. Therefore, the robustness against parameter mismatch is analyzed. It is depicted by Fig. 15 that the resistance mismatch has little effect on the proposed scheme. In the current loop, the inductance mismatch would only cause deviation around the resonant frequency, as shown by Fig. 15(a). In the disturbance loop, the inductance mismatch has little effect on frequency response, sufficient attenuation is yield at the resonant frequency, as shown by Fig. 15(b).

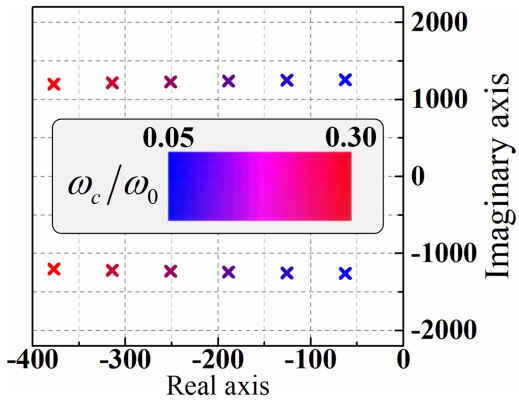

Fig. 16. Characteristic roots distribution law of $\Delta_2(z)=0$ with the change of ω_c ($\omega_0 = 1257$ rad/s).

Hence, it is verified that the proposed scheme exhibits sufficient compensation capability under parameter mismatch.

V. Analysis of Stability and Dead-Time Compensation Performance

In this section, first, the stability of the proposed scheme is analyzed. Then, the dead-time compensation capability of the proposed scheme is investigated from the perspective of anti-disturbance performance. Finally, the parameter tuning method is discussed.

A. Stability Analysis

According to (26) and (32), the characteristic equation of the proposed scheme is given by

$$\Delta(s) = \Delta_1(s)\,\Delta_2(s) \tag{33}$$

where

$$\Delta_1(s) = L_{dq}s^2+(K_p+R_s)s+K_i \tag{34}$$

$$\Delta_2(s) = s^2+2\omega_c s+\omega_0^2. \tag{35}$$

If all roots of $\Delta_1(s)$ and $\Delta_2(s)$ locate in the left-half of the s plane, the system is stable. Hence, based on the Routh criterion, the necessary and sufficient condition for system stability can be expressed as

$$\begin{cases} L_{dq}>0 \\ K_p+R_s>0 \\ K_i>0 \end{cases} \text{and} \begin{cases} 2\omega_c>0 \\ \omega_0^2>0 \end{cases}. \tag{36}$$

Since the values of K_p and K_i are always larger than zero, the condition shown in (36) can be further simplified as

$$\omega_c > 0. \tag{37}$$

According to (37), if the value of ω_c is set to be positive, the system is stable. Thus, it is indicated that the system stability is governed by $\Delta_2(s)$. To evaluate the effect of the RRC on system stability, the characteristic roots distribution law of $\Delta_2(s)$ is analyzed, as shown in Fig. 16. Since all roots locate in the left-half of the s plane, the system is stable. Besides, as ω_c increases,

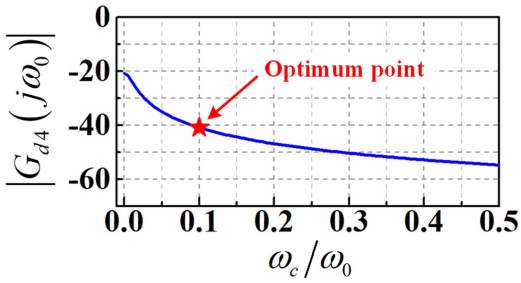

Fig. 17. Influence law of ω_c on the value of $|G_{d4}(j\omega_0)|$.

the poles move away from the imaginary axis. Hence, to ensure stability margin, the value of ω_c cannot be excessive small.

B. Dead-Time Compensation Performance

In order to evaluate the performance of the proposed dead-time compensation scheme, the capability of suppressing the dead time related disturbances is analyzed.

Substituting $s = j\omega_0$ into (32), it can be inferred that the value of $G_{d4}(j\omega_0)$ is zero. Hence, taking the speed ripple into account, the transfer function of the disturbance loop in the frequency domain can be approximated as

$$G_{d4}(j\omega_0) \approx G_{d4}(j(\omega_0+\Delta\omega)) = \frac{j(\omega_0+\Delta\omega)\left[(j(\omega_0+\Delta\omega))^2+\omega_0^2\right]}{\Delta(j(\omega_0+\Delta\omega))} \quad (38)$$

where $\Delta\omega = 12.57$ rad/s(5 r/min) is the frequency fluctuation.

Fig. 17 presents the influence law of ω_c on the value of $|G_{d4}(j\omega_0)|$. According to [15], the dead-time effect deteriorates at low speed. Therefore, the resonant frequency ω_0 is set to be 1257 rad/s (the speed is 500 r/min).

When ω_c is less than $0.1\omega_0$, the value of $|G_{d4}(j\omega_0)|$ drops sharply with the raise of ω_c. However, above $0.1\omega_0$, the contribution of increasing ω_c to the value of $|G_{d4}(j\omega_0)|$ tends to decrease. Besides, as ω_c raises, the peak gain of the RRC increases significantly, as shown in Fig. 13(a). High-frequency noise would be amplified consequently, leading to system instability. Hence, ω_c cannot be excessive large. Based on above analysis, ω_c is recommended to be $0.1\omega_0$ for a tradeoff between stability margin and antidisturbance performance.

C. Parameter Tuning Method

Based on above analysis, the parameter tuning method of the proposed scheme is summarized in Fig. 18. First, benefitting from the decoupling characteristic, the parameters of the control law can be tuned independent of the disturbance loop. Second, the parameter of the RRC is tuned for effective suppression of the dead time related voltage disturbances.

VI. Experiments

In order to validate the proposed scheme, an experimental test bench shown in Fig. 19 was built. TI TMS320F28335 DSP was utilized as the controller at 10 kHz sampling (switching)

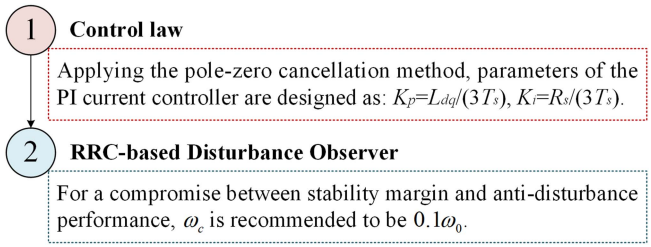

Fig. 18. Parameter tuning method of the proposed scheme.

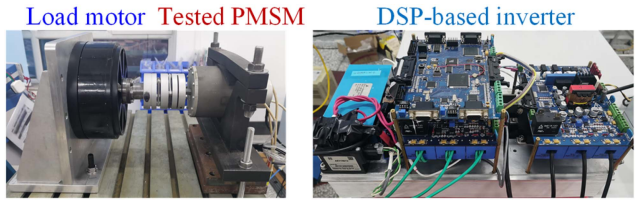

Fig. 19. Photo of test bench.

TABLE II
Parameters of PMSM

Parameter	Value	Parameter	Value
Rated power	0.55 kW	λ_f	0.0439 V·s
Rated speed	2000 r/min	L_d	3.044 mH
Rated current	7.07 Arms	L_q	3.044 mH
Pole pairs	4	R_s	0.08 Ω

frequency. The parameters of the tested 0.55 kW PMSM are given in Table II. The dc-link voltage of the inverter is 300 V, and the dead time T_d is set to be 3 μs. The tested PMSM was loaded with a motor operating in speed mode. According to [15], the dead-time effect deteriorates at low speed. Hence, the speed command is set to be 500 rpm to verify the proposed scheme.

In the following experiments, the tested PMSM operates in current mode, and the PI scheme (see Fig. 5 without G_{qrc}), the PIR-based scheme (see Fig. 5), the ESO-based scheme (see Fig. 6) and the proposed scheme (see Fig. 8) are implemented, respectively. The d-axis reference current is set to be zero. According to the parameter tuning method presented in Fig. 18, the parameters of the PI controller in four schemes are selected as: $K_p = 10.15$, $K_i = 266.67$. The QRC parameters of the PIR scheme are selected as $K_r = 500$, $\omega_c = 0.01\omega_0$. The bandwidth of the ESO is selected as $\omega_{\text{eso}} = 1000$ rad/s. And the RRC parameter of the proposed scheme is selected as: $\omega_c = 0.1\omega_0$.

A. Q-Axis Current Step Response

In the first experiment, the step response of the current loop is tested to validate the decoupling characteristic of the proposed scheme. Fig. 20 presents the experimental results with q-axis current reference changes from 3 to 8 A under four schemes. As shown in Fig. 20(a), the PI scheme donates smooth current step response, where both the rise time t_r and settling time t_s are 1.5 ms, and the overshoot σ is zero. However, due to inevitable coupling issue, significant overshoot and oscillation

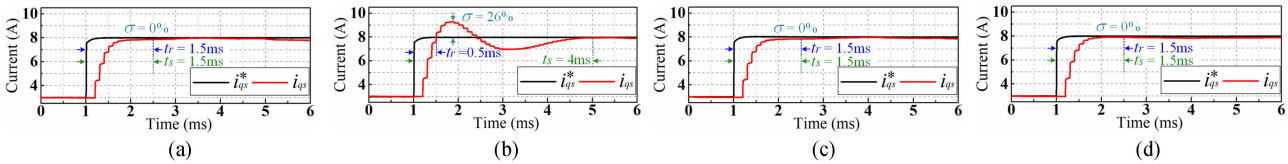

Fig. 20. Experimental results of q-axis current step responses under four schemes. (a) Proportional-integral. (b) Proportional-integral-resonant. (c) Extended-state observer. (d) Proposed scheme.

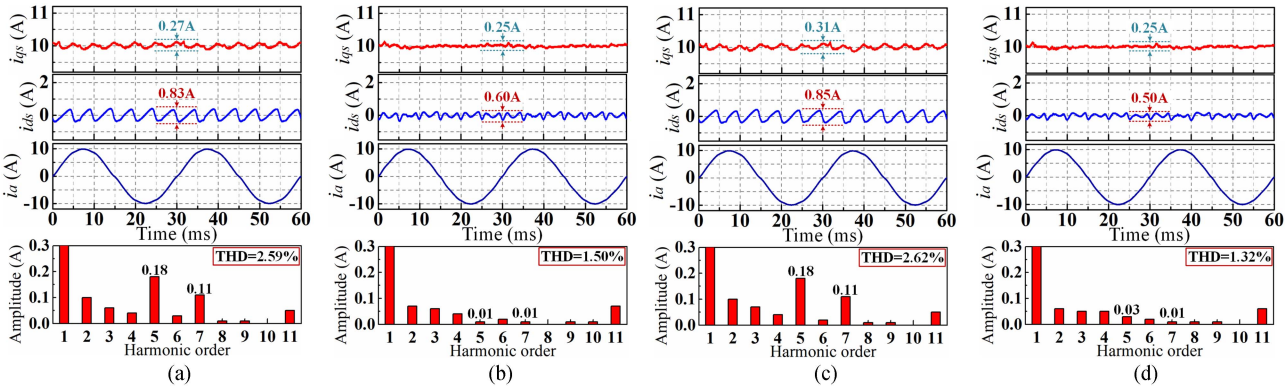

Fig. 21. Experimental results of steady-state current responses under four schemes at 500 r/min. From top to bottom: q-axis current, d-axis current, A-phase current, and its FFT spectrum. (a) Proportional-integral. (b) Proportional-integral-resonant. (c) Extended-state observer. (d) Proposed scheme.

are introduced in the PIR scheme, as shown in Fig. 20(b). Specifically, t_s is increased from 1.5 to 4 ms, while σ is up to 26%, which agrees well with the theoretical results shown in Fig. 11. As expected, both the ESO-based and proposed schemes virtually donate the same current step response as the PI scheme, as shown by Fig. 20(c) and (d). Hence, it is verified that in the proposed scheme, the current loop and voltage disturbance rejection loops are fully decoupled.

B. Steady-State Performance

To evaluate the steady-state compensation performance, Fig. 21 demonstrates the comparative experimental results of four schemes under 100% rated load (10A) at 500 r/min.

As shown in Fig. 21(a), due to the dead-time effect, there exist significant sixth harmonics in the q- and d-axis currents of the PI scheme, the fluctuations of which are up to 0.27 and 0.83A, respectively. The abundant harmonics in the d-axis current are due to the relatively large harmonics in the d-axis voltage error [see Fig. 3 and (7)]. In addition, the phase current is distorted especially in the zero-crossing region. As shown by the fast Fourier transform (FFT) spectrum, the phase current contain dominant fifth and seventh harmonics, which are 0.18 and 0.11A, respectively. The total harmonic distortion (THD) is 2.59%.

By the PIR scheme, the fluctuation of the q-axis current is reduced from 0.27 to 0.25A, while that of the d-axis current is reduced from 0.83 to 0.60 A, as shown in Fig. 21(b). Moreover, both the fifth and seventh harmonics of the phase current are reduced to as low as 0.01A. And THD is decreased from 2.59% to 1.50%. Hence, it is revealed that the PIR scheme can effectively suppress the dead-time effect.

It is revealed by Fig. 21(c) that the ESO virtually has little contribution on suppressing the current ripple, which is due to that the disturbance frequency (1257 rad/s) is beyond the ESO bandwidth (1000 rad/s). On the contrary, since the ESO could amplify the high frequency noise, both the current ripple and THD are even increased slightly compared with the PI scheme.

Compared with the PIR scheme, the proposed scheme can further reduce the d-axis current fluctuation, specifically, from 0.60 to 0.50 A, as shown in Fig. 21(d). Besides, as depicted in the FFT spectrum, by the proposed scheme, both the fifth and seventh harmonics are effectively suppressed, which show similar level as the PIR scheme. The THD is further reduced from 1.50% to 1.32%. Therefore, it is verified that the proposed scheme can achieve effective compensation of the dead-time effect. Besides, compared with the PIR scheme, the proposed scheme shows superior steady-state performance.

C. Parameter Mismatch

Since the resistant mismatch is negligible (see Fig. 15), only the effect of inductance mismatch is experimentally validated by detuning the estimated inductance online. Compared with the results in Fig. 21(d) (nominal inductance), the inductance mismatch donates similar current ripple level, while the THD is slightly increased, as shown by Fig. 22. Despite deterioration, the THD of the proposed scheme is still much lower than that of the PI scheme, showing robust compensation capability against parameter mismatch.

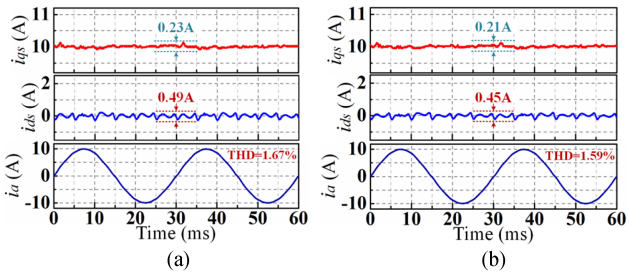

Fig. 22. Experimental steady-state responses of the proposed scheme under inductance mismatch at 500 r/min. From top to bottom: q-axis current; d-axis current; and A-phase current. (a) $\hat{L}_{dq} = 0.5L_{dq}$. (b) $\hat{L}_{dq} = 2L_{dq}$.

VII. Conclusion

In this article, a decoupled dead-time compensation method using the RRC-based disturbance observer was proposed for VSIs in PMSM drives. The proposed scheme can fully decouple the performances of the current control loop and dead-time compensation. Compared with the PIR scheme, the proposed scheme enables satisfactory dead-time compensation performance without distorting current response. Compared with the ESO, the proposed scheme donates superior tracking bandwidth and compensation capability. Compared with the QRC-based disturbance observer, the proposed RRC-based disturbance observer could guarantee system stability in full frequency range. The stability and dead-time compensation performance were analyzed in detail.

The proposed scheme was experimentally validated on a 0.55 kW PMSM platform. Experimental results demonstrate that compared with the PI, ESO, and PIR schemes, the proposed scheme enables superior dead-time compensation performance. In addition, compared with the PIR scheme, the proposed scheme achieves same current step response as the PI scheme without causing overshoot and oscillation.

References

[1] A. R. Munoz and T. A. Lipo, "Online dead-time compensation technique for open-loop PWM-VSI drives," *IEEE Trans. Power Electron.*, vol. 14, no. 4, pp. 683–689, Jul. 1999.

[2] D.-H. Lee and J.-W. Ahn, "A simple and direct dead-time effect compensation scheme in PWM-VSI," *IEEE Trans. Ind. Appl.*, vol. 50, no. 5, pp. 3017–3025, Sep./Oct. 2014.

[3] Z. Zhang and L. Xu, "Dead-time compensation of inverters considering snubber and parasitic capacitance," *IEEE Trans. Power Electron.*, vol. 29, no. 6, pp. 3179–3187, Jun. 2014.

[4] N. Bedetti, S. Calligaro, and R. Petrella, "Self-commissioning of inverter dead-time compensation by multiple linear regression based on a physical model," *IEEE Trans. Ind. Appl.*, vol. 51, no. 5, pp. 3954–3964, Sep./Oct. 2015.

[5] Z. Chen, T. Shi, Y. Cao, C. Li, and Y. Yan, "An accurate inverter nonlinearity compensation method for IPMSM torque estimation based on numerical fitting," *IEEE J. Emerg. Sel. Top. Power Electron.*, vol. 11, no. 2, pp. 2126–2138, Apr. 2023.

[6] C. Shang, M. Yang, J. Long, D. Xu, J. Zhang, and J. Zhang, "An accurate VSI nonlinearity modeling and compensation method accounting for DC-link voltage variation based on LUT," *IEEE Trans. Ind. Electron.*, vol. 69, no. 9, pp. 8645–8655, Sep. 2022.

[7] G. Liu, D. Wang, Y. Jin, M. Wang, and P. Zhang, "Current-detection-independent dead-time compensation method based on terminal voltage A/D conversion for PWM VSI," *IEEE Trans. Ind. Electron.*, vol. 64, no. 10, pp. 7689–7699, Oct. 2017.

[8] Y.-K. Lin and Y.-S. Lai, "Dead-time elimination of PWM-controlled inverter/converter without separate power sources for current polarity detection circuit," *IEEE Trans. Ind. Electron.*, vol. 56, no. 6, pp. 2121–2127, Jun. 2009.

[9] Q. Yan, R. Zhao, X. Yuan, W. Ma, and J. He, "A DSOGI-FLL-based dead-time elimination PWM for three-phase power converters," *IEEE Trans. Power Electron.*, vol. 34, no. 3, pp. 2805–2818, Mar. 2019.

[10] T. Qiu, X. Wen, and F. Zhao, "Adaptive-linear-neuron-based dead-time effect compensation scheme for PMSM drives," *IEEE Trans. Power Electron.*, vol. 31, no. 3, pp. 2530–2538, Mar. 2016.

[11] Z. Zhou, C. Xia, Y. Yan, Z. Wang, and T. Shi, "Disturbances attenuation of permanent magnet synchronous motor drives using cascaded predictive-integral-resonant controllers," *IEEE Trans. Power Electron.*, vol. 33, no. 2, pp. 1514–1527, Feb. 2018.

[12] Z. Pan, F. Dong, J. Zhao, L. Wang, H. Wang, and Y. Feng, "Combined resonant controller and two-degree-of-freedom PID controller for PMSLM current harmonics suppression," *IEEE Trans. Ind. Electron.*, vol. 65, no. 9, pp. 7558–7568, Sep. 2018.

[13] H. Yi, F. Zhuo, and F. Wang, "Analysis about overshoot peaks appearing in the current loop with resonant controller," *IEEE J. Emerg. Sel. Top. Power Electron.*, vol. 4, no. 1, pp. 26–36, Mar. 2016.

[14] C. Xia, B. Ji, and Y. Yan, "Smooth speed control for low-speed high-torque permanent-magnet synchronous motor using proportional-integral-resonant controller," *IEEE Trans. Ind. Electron.*, vol. 62, no. 4, pp. 2123–2134, Apr. 2015.

[15] Z. Tang and B. Akin, "Suppression of dead-time distortion through revised repetitive controller in PMSM drives," *IEEE Trans. Energy Convers.*, vol. 32, no. 3, pp. 918–930, Sep. 2017.

[16] M. Hu, W. Hua, G. Ma, S. Xu, and W. Zeng, "Improved current dynamics of proportional-integral-resonant controller for a dual three-phase FSPM machine," *IEEE Trans. Ind. Electron.*, vol. 68, no. 12, pp. 11719–11730, Dec. 2021.

[17] Z. Song, Y. Wang, and T. Shi, "A dual-loop predictive control structure for permanent magnet synchronous machines with enhanced attenuation of periodic disturbances," *IEEE Trans. Power Electron.*, vol. 35, no. 1, pp. 760–774, Jan. 2020.

[18] N. Urasaki, T. Senjyu, K. Uezato, and T. Funabashi, "An adaptive dead-time compensation strategy for voltage source inverter fed motor drives," *IEEE Trans. Power Electron.*, vol. 20, no. 5, pp. 1150–1160, Sep. 2005.

[19] X. Hao and Y. Luo, "An SMC-ESO based distortion voltage compensation strategy for PWM VSI of PMSM," *IEEE J. Emerg. Sel. Top. Power Electron.*, vol. 10, no. 5, pp. 5686–5697, Oct. 2022.

[20] M. Zhao and Q. Ge, "Grid-side harmonic current suppression based on carrier phase-shifted PWM and extended state observer for high-power multiple parallel 3L-ANPC rectifier," *IEEE Trans. Ind. Electron.*, vol. 71, no. 6, pp. 5399–5410, Jun. 2024.

[21] M. Tian, B. Wang, Y. Yu, Q. Dong, and D. Xu, "Discrete-time repetitive control-based ADRC for current loop disturbances suppression of PMSM drives," *IEEE Trans. Ind. Informat.*, vol. 18, no. 5, pp. 3138–3149, May 2022.

[22] Y. Chen, X. Zhang, J. Yang, L. Yan, and R. Deng, "Smooth and robust current control of PMSMs with decoupling-type extended state observers," *IEEE Trans. Ind. Electron.*, vol. 71, no. 9, pp. 10377–10388, Sep. 2024, doi: 10.1109/TIE.2023.3342305.

Jiewen Lang received the B.Sc. and M.Sc. degrees in electrical engineering in 2018 and 2020, respectively, from Harbin Institute of Technology, Harbin, China, where he is currently working toward the Ph.D. degree in electrical engineering. His research interests include analytical modeling of electric machines, axial-flux magnetic-geared double-rotor machines for hybrid electric vehicles, and ac motor drives.

Chengde Tong (Member, IEEE) received the B.Sc., M.Sc., and Ph.D. degrees in electrical engineering from Harbin Institute of Technology, Harbin, China, in 2007, 2009, and 2013, respectively.

He is currently a Professor with the Department of Electrical Engineering, Harbin Institute of Technology. He is the author or coauthor of more than 60 published papers. His research interests include electric drives and energy management of hybrid electric vehicles, free-piston Stirling engines, and permanent-magnet linear machines.

Yuhong Zheng received the B.Sc. degree in electrical engineering in 2023 from Harbin Institute of Technology, Harbin, China, where he is currently working toward the Ph.D. degree in electrical engineering.

His research interests include suppression of torque ripple, control strategy of permanent-magnet linear synchronous machines, and ac motor drives.

Jingang Bai (Member, IEEE) received the B.Sc. degree from Harbin University of Science and Technology, Harbin, China, and the M.Sc. and Ph.D. degrees from Harbin Institute of Technology, Harbin, China, in 2009, 2011, and 2016, respectively, all in electrical engineering.

He is currently a Professor with the Department of Electrical Engineering, Harbin Institute of Technology. He is the author or coauthor of more than 50 published technical papers. He is the holder of 27 Chinese invention patents. His research interests include brushless compound-structure permanent-magnet synchronous machines used for hybrid electric vehicles, high power density linear machines used for the Stirling engine system, and less or no rare-earth PM machines used for electric vehicles.

Ping Zheng (Senior Member, IEEE) received the B.Sc., M.Sc., and Ph.D. degrees from Harbin Institute of Technology, Harbin, China, in 1992, 1995, and 1999, respectively, all in electrical engineering.

Since 1995, she has been with Harbin Institute of Technology, where she has been a Professor since 2005. She is the author or coauthor of more than 320 published refereed technical papers and four books. She is the holder of 80 Chinese invention patents. Her current research interests include electric machines and control, hybrid electric vehicles, and the cloud computing of electric machine system.

Dr. Zheng was a recipient of more than 40 technical awards, including the "China Youth Science and Technology Award" from the Organization Department of the Communist Party of China in 2009, the "National Science Foundation for Distinguished Young Scholars of China" from the National Natural Science Foundation of China in 2013, and the "National High-Level Talent Program" from the Ministry of Education of China in 2014.